

# Modelling Inter-pixel Spatial Variation of Surface Urban Heat Island Intensity

Yanhua Chen

The University of Hong Kong

Wendy Y. Chen (✉ [wychen@hku.hk](mailto:wychen@hku.hk))

The University of Hong Kong <https://orcid.org/0000-0001-8235-6446>

Raffaele Laforzezza

Department of Agricultural and Environmental Sciences, University of Bari

---

## Research Article

**Keywords:** pixel-level sharpening enhancement, MODIS, inter-pixel thermodynamics, inter-pixel landscape heterogeneity

**Posted Date:** December 14th, 2021

**DOI:** <https://doi.org/10.21203/rs.3.rs-1105672/v1>

**License:** © ⓘ This work is licensed under a Creative Commons Attribution 4.0 International License.

[Read Full License](#)

---

1 **Modelling inter-pixel spatial variation of Surface Urban Heat Island Intensity**

2

3 Yanhua Chen<sup>a</sup>, Wendy Y. Chen<sup>a,\*</sup>, Raffaele Laforzezza<sup>b</sup>

4 <sup>a</sup>Department of Geography, The University of Hong Kong, Pokfulam Road, Hong Kong

5 <sup>b</sup> Department of Agricultural and Environmental Sciences, University of Bari Aldo Moro, Via

6 Amendola 165/A 70126 Bari, Italy

7

8

9

10

11

12

13 \* Contact information of the corresponding author, Dr. Wendy Y. Chen

14 Mail address: Pokfulam Road, Hong Kong

15 Email: [wychen@hku.hk](mailto:wychen@hku.hk)

16 **Abstract**

17 **Context**

18 *Surface urban heat island intensity (SUHII) is a classical measure depicting urban heat island*  
19 *phenomenon via remotely sensed thermal infrared data and comparison of urban and rural*  
20 *land surface temperatures (LST), which are not only sensitive to the selection of*  
21 *pixels/measurements representative of urban and rural areas, but also overlook the pixel-level*  
22 *SUHII variation and thermodynamics associated with heterogeneous urban landscape.*  
23 *Accounting inter-pixel landscape heterogeneity in the quantification of SUHII would capture*  
24 *inter-pixel thermodynamics and reveal complicated micro-thermal situations, thus contribute*  
25 *to rigorous assessment of potential heat risks at micro-pixel scale and tailored design of*  
26 *mitigation strategies.*

27 **Objectives**

28 *This study develops a new measurement of SUHII,  $\widehat{SUHII}_{en}$ , using pixel-based sharpening*  
29 *enhancement method. It integrates a pixel's LST magnitude that reflects a city's overall thermal*  
30 *context with its local SUHII that takes the landscape variations and cognate thermal*  
31 *interactions of neighboring pixels into account. Thus, it is responsive to inter-pixel landscape*  
32 *heterogeneity while avoiding urban-rural demarcation.*

33 **Methods**

34  *$\widehat{SUHII}_{en}$  is constructed using Moderate Resolution Imaging Spectroradiometer (MODIS) LST*  
35 *product for Guangzhou (south China) in the summer season of 2015 through cloud-based*

36 *Google Earth Engine (GEE) platform. The effectiveness of  $SUHI\widehat{I}en$  is tested using a*  
37 *bivariate choropleth map and Gaussian density curve with stepwise increments of the thermal*  
38 *influence from neighboring pixels on the center pixels.*

### 39 **Results**

40 *We found that (1) local SUHI variations are sensitive to the spatial composition and*  
41 *configuration of a center pixel's land use type and that of its eight neighbors; (2)  $SUHI\widehat{I}en$*   
42 *makes more pronounced those spots that are not only heat per se (with higher original LST),*  
43 *but also receive additional heat load emitted from directly adjacent pixels due to land use*  
44 *homogeneity; (3) the effectiveness of  $SUHI\widehat{I}en$  could be demonstrated by Gaussian density*  
45 *curve with stepwise increments of the thermal influence from neighboring pixels.*

### 46 **Conclusions**

47 *This paper proposed an innovative attempt to quantify a new SHUI indicator,  $SUHI\widehat{I}en$ ,*  
48 *which models inter-pixel spatial variation of SHUI and highlights how neighboring pixels'*  
49 *homogenous/heterogeneous land use and associated thermal properties could affect center*  
50 *pixels' thermal characteristics via either reinforcement or mitigation of heat load.*

51

52 **Keywords:** pixel-level sharpening enhancement, MODIS, inter-pixel thermodynamics, inter-  
53 pixel landscape heterogeneity

54

55

56 **Introduction**

57 Surface urban heat island intensity (SUHII) has long been recognized as an efficient and reliable  
58 way to depict urban heat island (UHI) phenomenon (Li et al. 2018; Rao 1972; Stewart and Oke  
59 2012; Zhou et al. 2019), one of the major environmental problems in the 21st century facing  
60 human society across the globe. SUHII uses extensive thermal infrared remote sensing data  
61 (land surface temperature, i.e. LST) derived from multiple airborne or satellite sources to  
62 measure the radiative temperature differences between continuous urban and surrounding non-  
63 urban surfaces with similar geographic features (Peng et al. 2012; Voogt and Oke 2003; Zhang  
64 and Cheng 2019; Zhou and Chen 2018), instead of relying on ground-based meteorological  
65 monitoring data which are usually spatially scarce and sparsely distributed (Li and Li 2020;  
66 Oke 1982; Smoliak et al. 2015; Zhou and Chen 2018). With the advent and rapid advancements  
67 of thermal remote sensing technology and easy accessibility to a large corpora of remote  
68 sensing data with wall-to-wall coverage of land surface and continuous temporal operation,  
69 SUHII has gained increasing attention and wide application in recent decades (Li et al. 2020a;  
70 Lu et al. 2020; Meng et al. 2018; Rasul et al. 2017; Shen et al. 2020; Zhou and Chen 2018). It  
71 has greatly improved the scientific understanding of the characteristics of surface urban heat  
72 island phenomenon and associated driving forces (Buyantuyev and Wu 2010; Lai et al. 2018;  
73 Streutker 2002; Tran et al. 2006), and provide useful information for designing various  
74 anthropogenic interventions to mitigate heat risks in tandem with cognate environmental and  
75 public health problems (Bonafoni et al. 2017; Deilami et al. 2018; Jenerette et al. 2016; Peng  
76 et al. 2020).

77 The most common and widely adopted approach for quantifying SUHII is to compare LST  
78 differences between urban and surrounding rural/reference areas (Li et al. 2020a; Lu et al. 2020;  
79 Peng et al. 2012; Rasul et al. 2017; Schwarz et al. 2011). While this SUHII measurement could  
80 provide useful UHI information at various spatio-temporal scales (Li and Li 2020) and facilitate  
81 inter-city comparison (Shen et al. 2020), it is obviously sensitive to the selection of  
82 representative pixels which can adequately delineate urban and rural/reference areas (Deilami  
83 et al. 2018; Li et al. 2018; Li et al. 2020a; Streutker 2002). The empirical differentiation  
84 between urban and rural areas is indeed, in most cases, fuzzy and inconsistent (Li et al. 2012;  
85 Rajasekar and Weng 2009; Stewart and Oke 2012). Moreover, the quantification of SHUII  
86 based on urban-rural comparison commonly views UHI as a constant and uniform phenomenon  
87 at coarse scales like the whole urbanized area, and thus tends to ignore intra-urban  
88 thermodynamics and structural heterogeneity resulted from highly complex biophysical and  
89 anthropogenic characteristics (Guo et al. 2015; Li et al. 2017; Rajasekar and Weng 2009; Yu et  
90 al. 2021).

91 To minimize distorted interpretations of SUHII brought by varying urban-rural definitions and  
92 quantitatively investigate the intra-city dynamics of SUHII, statistical modelling techniques  
93 have been proposed for SUHII quantification. References (Streutker 2002, 2003; Tran et al.  
94 2006) introduced a two-dimensional Gaussian surface fit model to simulate the multiple  
95 features of SUHII. While this technique can generate more UHI information about magnitude  
96 and spatial extents, it requires a prior extraction of a planar rural background upon which a  
97 Gaussian surface can be superimposed to model the spatial dynamic of SUHII across urban  
98 areas (Anniballe et al. 2014; Lai et al. 2021; Pereira Filho and Karam 2016; Yang et al. 2019),

99 and thus uncertainties might be induced by different definitions of rural extents (Li et al. 2019).  
100 Besides, non-parametric kernel convolution model has been suggested, which can  
101 quantitatively characterize SUHII over a continuous surface without the need to delineate  
102 urban-rural dichotomy (Rajasekar and Weng 2009; Weng et al. 2011). This modelling  
103 technique computes SUHII of each pixel as the difference between the maximum and the mean  
104 LST value derived via smoothing LST values together with adjacent pixels. It can capture  
105 continuous SUHII over the entire study area, reduce the impact of missing pixels  
106 (Keramitsoglou et al. 2011), and avoid potential biases caused by urban-rural definitions (Zhou  
107 and Chen 2018). Nonetheless, this smoothing process tends to average the thermal property of  
108 center pixel with neighboring pixels, instead of accounting the thermodynamics between the  
109 center pixels and their neighboring pixels. Another group of approaches employ linear  
110 regression function to quantify SUHII via the examination of the relationships between LST  
111 and various metrics of biophysical or socioeconomic factors. These include, but are not limited  
112 to, characteristics of land use and land cover (Li et al. 2012), impervious surface abundance (Li  
113 et al. 2018; Yang et al. 2020), normalized difference vegetation index (Sekertekin and  
114 Zadbagher 2021), population density and distribution (Xiao et al. 2008). While regression  
115 models can generally capture the spatial variations of SUHII over all the scales from pixel to  
116 global through establishing relationships between SUHI and driving factors (Lai et al. 2021),  
117 they require a combined input of LST data and related biophysical and socioeconomic data,  
118 which might introduce more uncertainties such as a mismatch of spatial units for LST and  
119 relevant driving factors (Xiao et al. 2008). Meanwhile, these linear regression models  
120 commonly ignore the spatial non-stationary effect of driving factors on SUHI thus might not

121 be able to reflect local SUHII variations (Guo et al. 2020; Li et al. 2020b; Weng et al. 2011;  
122 Zhao et al. 2018).

123 The inherent spatial complexity and heterogeneity of urban surface and associated thermal  
124 properties across the whole city creates a limitless array of thermal contexts and microclimate  
125 systems (Buyantuyev and Wu 2010; Oke 1982; Weng et al. 2011; Xiao et al. 2008), which  
126 necessitates site-specific assessment of UHI so that tailored mitigation approaches can be  
127 adequately designed (Bonafoni et al. 2017; Deilami et al. 2018; Zhao et al. 2018). Therefore, a  
128 key issue would be how to use LST data retrieved from thermal infrared images at the pixel  
129 scale to quantify and characterize evident intra-city SUHII variations (Keramitsoglou et al.  
130 2011; Weng 2009). In this study, we propose to use a pixel-based sharpening enhancement  
131 method to quantify an enhanced SUHII ( $SUHII_{en}$ ). This new indicator aims to highlight pixel-  
132 level SUHII variations across the whole urban area through explicitly defining the heating or  
133 cooling influences from neighboring pixels' on center pixel's SUHI based on a kernel  
134 convolution process. The main objective of this paper therefore is to illustrate the computation  
135 of this  $SUHII_{en}$  indicator and verify its effectiveness via a demonstrative case study using  
136 Moderate Resolution Imaging Spectroradiometer (MODIS) land surface temperature data and  
137 land use data for Guangzhou (southern China) in the summer season of 2015 through the cloud-  
138 based Google Earth Engine (GEE) platform (Gorelick et al. 2017).

### 139 **Sharpening enhancement approach**

140 Different from the pan-sharpening concept in remote sensing image processing aiming to obtain  
141 multi-spectral images of high-resolution by fusing panchromatic images and multi-spectral

142 images (Kwarteng and Chavez 1989; Ma et al. 2020), the sharpening enhancement approach in  
143 this study refers specifically to as a technique to detect and enhance the attributes of interest  
144 (SUHII in our case study) from a single image source for future processing, i.e. detection,  
145 recognition, visualization and analysis. This technique could detect the edge and enhance the  
146 image intensity variation by adding the scaled edge information into the spatial domain (instead  
147 of homogenization of image intensity), so as to increase the contrast, explicitly extract the  
148 boundary of the image segment, and facilitate the recognition of the target area (Jeevakala 2018).  
149 Nonetheless, in line with (Zhan et al. 2013) who defined thermal sharpening as “any procedure  
150 through which (remotely sensed) thermal images are enhanced or made clearer for the purpose  
151 of interpretation”, this study extends beyond this definition of pan-sharpening of thermal  
152 images from multiple satellite/aircraft platforms (Duan and Li 2016) to the enhancement of  
153 thermal images from one satellite sensor with an aim to highlight the spatial variation of SUHII  
154 across the urban-periphery-rural continuum of a study area in avoidance of various uncertainties  
155 and tradeoffs amongst different temporal, spatial, and spectral resolutions of images (Feng et  
156 al. 2015; Zhan et al. 2013).

157 To realize sharpening enhancement, many algorithms have been developed in order to highlight  
158 the difference, enhance edge information of the image, and differentiate intensity change area  
159 in a local context (Torre and Poggio 1986). The first order derivatives, such as Roberts operator  
160 (Roberts 1963), Sobel operator (Sobel and Feldman 1968), and Prewitt operator (Prewitt 1970),  
161 could filter and detect the magnitude difference of neighboring pixels, and point out the rate  
162 and direction of intensity variation. The second order derivatives, such as Laplacian operator  
163 or Laplacian of Gaussian (LoG) operator (Marr and Hildreth 1980), Canny operator (Canny

164 1986), as well as Haralick operator (Haralick 1987), could give stronger responses in finding  
165 maximum gradient of intensity changes and isolated points (Dhal et al. 2019). Both Laplacian  
166 operator and LoG operator (with the same kernel in a 3x3 moving window) have been widely  
167 used for detecting contrast between the target pixel and its surrounding (Ratcliffe 1997). Canny  
168 operator and Haralick operator are targeted at optimal edge detection using non-maximum  
169 suppression and bi-cubic polynomial fitting function, respectively. They tend to focus only on  
170 the most significant edges/changes and considerable local information would be neglected.

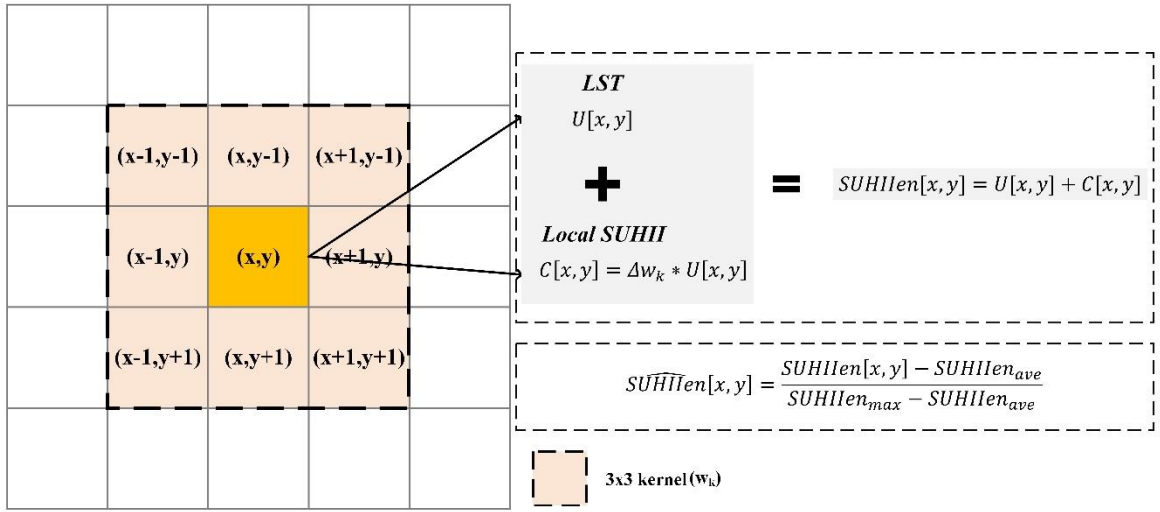
171 Besides its wide applications in digital image processing, sharpening enhancement techniques  
172 have been employed to retrieve detailed information from remotely sensed images, such as land  
173 surface segmentation and classification (Yu et al. 2018), geological lineament identification  
174 (Basu 2002; Han et al. 2018), detection of groundwater zones (Mahmoud and Alazba 2016),  
175 reef extraction (Li and Wang 2013), enumeration of olive trees (Waleed et al. 2020), and crop  
176 field monitoring (Fu et al. 2008). That being said, the application of sharpening enhancement  
177 techniques to characterize SUHII variations across continuous spatial terrains is currently  
178 lacking, which promises to reveal more detailed information about SUHI such as boundary and  
179 center position, spatial extent, so as to provide tailor-designed planning guideline for mitigating  
180 the negative impacts of UHI (Peng et al. 2020).

181

## 182 **Method**

183 The proposed process of  $\widehat{SUHII}en$  quantification is illustrated in Fig. 1. Firstly, sharpening  
184 local SUHI variation  $C$  (local SHUII) is computed for each pixel  $(x, y)$  with respect to its  
185 neighbors within a 3x3 window using Laplacian operator, which detects and quantifies local

186 SUHI variation patterns within this moving window for each pixel. This process is explained  
 187 in Section A. Then the resulted local SUHII  $C[x, y]$  is combined with the original LST of each  
 188 pixel  $U[x, y]$  to derive an enhanced SHUII (SHUII<sub>en</sub>), and SHUII<sub>en</sub> is normalized within the  
 189 boundary of the city for easy interpretation to obtain  $\widehat{SUHII}_{en}$ . More details are given in  
 190 Section B.



192 Fig. 1. An overview of the sharpening enhancement method for  $\widehat{SUHII}_{en}$  computation

193

194 *A. Sharpening local SUHII via Laplacian operator*

195 Let a digital LST image be  $U: \Omega \rightarrow \mathbb{R}$ , where  $\Omega \subset \mathbb{R}^2$  is image support and the continuous LST  
 196 image is  $u$ . and let the pixel value be  $U[x, y]$  at location  $(x, y)$  at a specific time. The first  
 197 derivative is the same as the gradient of the temperature processing in space, which is given as:

198 
$$\nabla u = \left[ \frac{\partial u}{\partial x}, \frac{\partial u}{\partial y} \right] \quad (1)$$

199 where the magnitude of the gradient is given as:

200

201 
$$|\nabla u| = \sqrt{\left(\frac{\partial u}{\partial x}\right)^2 + \left(\frac{\partial u}{\partial y}\right)^2} \quad (2)$$

202 and the direction is:

203 
$$\theta = \tan^{-1}\left(\frac{\partial u}{\partial y} / \frac{\partial u}{\partial x}\right) \quad (3)$$

204

205 For image processing, the discrete image of  $\nabla U$  in Eq(1) can be calculated by finite-difference

206 approximations of the orthogonal vector  $x$  and  $y$ . The simple equation for the gradient and

207 direction of a digital image considering the forward difference is shown as follows:

208

209 
$$\nabla U \approx [U[x + 1, y] - U[x, y], U[x, y + 1] - U[x, y]] \quad (4)$$

210

211 where the magnitude of the gradient is given by:

212 
$$|\nabla U| = \sqrt{(U[x + 1, y] - U[x, y])^2 + (U[x, y + 1] - U[x, y])^2} \quad (5)$$

213 and the direction is:

214 
$$\theta = \tan^{-1} \frac{U[x, y + 1] - U[x, y]}{U[x + 1, y] - U[x, y]} \quad (6)$$

215 The second derivative is the change rate in the first derivative. The Laplacian operator  $\nabla^2$ , which

216 can also be represented by  $\Delta$ , of function  $u$  is shown as:

217 
$$\nabla^2 u = \frac{\partial^2 u}{\partial x^2} + \frac{\partial^2 u}{\partial y^2} + \frac{\partial^2 u}{\partial x \partial y} + \frac{\partial^2 u}{\partial y \partial x} \quad (7)$$

218 which has

219 
$$\Delta = \nabla \cdot \nabla \tag{8}$$

220 While for the first derivative SUHI variation is localized at its maximum or minimum value,  
 221 for the second derivative it results in the zero (or the passage through zero) and has a positive  
 222 sign in the zone of ascending ramp and negative in the zone of descending ramp. The second  
 223 derivative can locate the edge pixels corresponding to the pixel where the rising or falling side  
 224 of  $\nabla^2 u$  passes through the zero (from positive to negative and vice versa), thus detect local  
 225 SUHI intensity variation.

226 The second derivative can be approximated by difference equations for the center pixel  $U[x, y]$ ,  
 227 which is given by:

228 
$$\begin{aligned} \Delta U \approx & (U[x + 1, y] + U[x - 1, y] - 2U[x, y]) \\ & + (U[x, y + 1] + U[x, y - 1] - 2U[x, y]) \\ & + (U[x + 1, y + 1] + U[x - 1, y - 1] - 2U[x, y])^{(9)} \\ & + (U[x + 1, y - 1] + U[x - 1, y + 1] - 2U[x, y]) \end{aligned}$$

229 Local SUHII is quantified considering simultaneously the center pixel  $U_c$  and its eight first-  
 230 order neighboring pixels  $U_n$  within moving window through a 3x3 Laplacian kernel.  $w_k$  is  
 231 defined as:

232 
$$\Delta w_k = \begin{bmatrix} 1/8 & 1/8 & 1/8 \\ 1/8 & -1 & 1/8 \\ 1/8 & 1/8 & 1/8 \end{bmatrix} \tag{10}$$

233 In this study, the direct thermal impacts from eight first-order neighbors on the center pixel is  
 234 considered. We exclude higher-order neighbors (such as second-order and third-order  
 235 neighbors), mainly due to their indirect thermal impacts on the center pixel.

236  $C[x, y]$  is used represent the magnitude of local SUHII between the center pixel,  $U_c$ , and its  
237 neighboring pixels,  $U_n$ , taking into account of the thermal influence exerted by  $U_n$ . It is  
238 calculated through kernel convolution.

$$239 \quad C[x, y] = \Delta w_k * U[x, y] \quad (11)$$

240  $C[x, y]$  has three possible results, showing different SUHII patterns and changes.

241 (1)  $C > 0$ , indicating that neighboring pixels exert a heating impact onto the center pixel  
242 within the given window, and the value of  $C$  denotes the strength of this heating impact.

243 (2)  $C < 0$ , indicating that neighboring pixels exert a cooling impact onto the center pixel  
244 within the given window, and the value of  $C$  denotes the strength of this cooling impact.

245 (3)  $C = 0$ , showing that there is no SUHII change with the given window, and thus no  
246 interactive influence between neighboring and center pixels.

247

#### 248 *B. Enhancement of local SUHII: $SUHII_{en}$*

249 Within the urban boundary, local SUHII is further enhanced to be  $SUHII_{en}$  by adding  $C$   
250 variation with  $U$  variation which reflect the overall background thermal context, to obtain  
251  $SUHII_{en}$ .

$$252 \quad SUHII_{en}[x, y] = U[x, y] + C[x, y] \quad (12)$$

253 This  $SUHII_{en}$  combines the thermal impacts introduced by neighboring pixels into the center  
254 pixel's original LST. It integrates two dimensions of UHI, the original LST (reflecting the  
255 overall background context across a city) and local SUHI variation (reflecting the influence of

256 neighboring land use), so as to highlight potential heat/cold islands associated with the land use  
257 homogeneity (such as hot centers surrounded by hotter neighbors, and cold centers surrounded  
258 by colder neighbors) and moderate heat/cold islands associated with land use heterogeneity  
259 (such as hot centers surrounded by cold neighbors, and cold centers surrounded by hot  
260 neighbors).

261 For easy interpretation, a normalized  $SUHIIen$  ( $\widehat{SUHIIen}$ ) is computed by

262

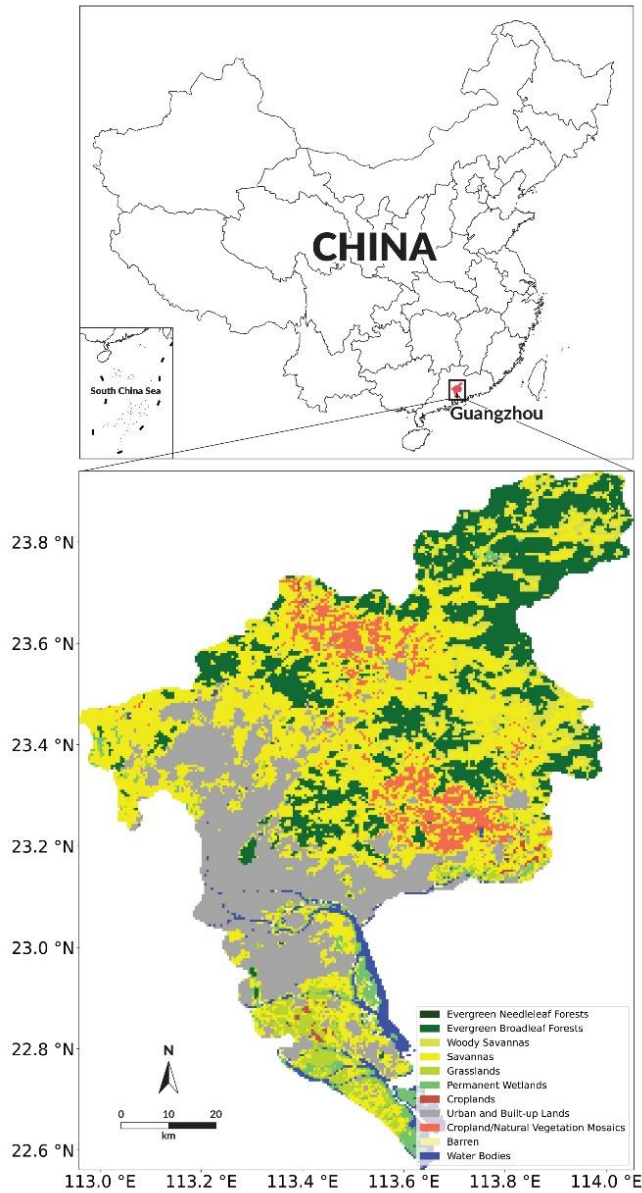
$$263 \quad \widehat{SUHIIen}[x, y] = \frac{SUHIIen[x, y] - SUHIIen_{ave}}{SUHIIen_{max} - SUHIIen_{ave}} \quad (13)$$

264 where  $SUHIIen_{max}$  is the maximum value of  $SUHIIen$ , and  $SUHIIen_{ave}$  is the mean value  
265 of  $SUHIIen$  across the whole study city. The value of  $\widehat{SUHIIen}$  ranges between [-1, 1]. This  
266  $\widehat{SUHIIen}$  can be applied to detect the intensity of UHI and urban cold islands (UCI) at  
267 varying scales. And the cloud-based Google Earth Engine (GEE) provides an appropriate  
268 platform for executing all computations and visualizing  $\widehat{SUHIIen}$  in a timely manner  
269 (Gorelick et al. 2017).

## 270 **An experimental case**

271 Guangzhou city, located in the Pearl River Delta, southeast China, is selected for a case study  
272 (Fig. 2). Being a typical city experiencing rapid urbanization, its UHI and cognate impacts on  
273 citizen's daily life has been of great concern (Chao et al. 2020). Using the standard LST product  
274 (MOD11A1) generated by the Moderate Resolution Imaging Spectroradiometer (MODIS)  
275 onboard the NASA Terra and Aqua Earth Observation System satellites,  $\widehat{SUHIIen}$  is

276 computed on GEE platform and tested using MODIS land use and land cover product  
277 (MCD12Q1).



278

279 Fig. 2. The study area and land cover of Guangzhou in 2015

280 MOD11A1 LST data at 1 km resolution have been verified and extensively used in SUHI  
281 studies (Rajasekar and Weng 2009; Wan et al. 2004; Wang et al. 2019; Wang et al. 2008). In  
282 this experimental case, daytime (10:30 h local time) observations in the summer season (from

283 June 01 to August 31) of 2015 are selected, as the UHI effect is most pronounced in the summer  
284 season and thus requires considerable policy attention (Zhao et al. 2014). Following a recent  
285 empirical study (Chakraborty and Lee 2019), two criteria are applied in LST data screening: an  
286 average LST error of less than or equal to 3K, and cloud-free. The seasonal LST is then  
287 computed via arithmetically averaging all LST records for each pixel for the study period. This  
288 could provide a simple representation of summer LST patterns and also eliminate short term  
289 fluctuations in weather and land surface conditions (Li and Dong 2009; Wang et al. 2019).

290 MCD12Q1 product for 2015 at  $500m \times 500m$  resolution is used to test the effectiveness of  
291  $\widehat{SUHI}_{Ten}$  in depicting pixel-level thermal variations. To match with LST data and  $\widehat{SUHI}_{Ten}$   
292 results, MAC12Q1 product is upscaled to a spatial resolution of 1 km using median aggregation  
293 method (Bian and Butler 1999). MAC12Q1 product contains 17 land cover types based on the  
294 classification system of the Annual International Geosphere-Biosphere Programme. In  
295 Guangzhou, a total of 11 land cover types are finally extracted (Fig. 2). In order to streamline  
296  $\widehat{SUHI}_{Ten}$  validation, all land cover types are re-grouped into buildings and impervious surface  
297 (labeled B: including “urban and built-up land”, and “barren land”), green vegetation (labeled  
298 G: including “evergreen needleleaf forests”, “evergreen broadleaf forests”, “woody savannas”,  
299 “savannas”, “grasslands”, “permanent wetlands”, “croplands”, and “cropland/natural  
300 vegetation mosaics”), and others (covering “water bodies”). The last group “water bodies” is  
301 excluded in our analysis. Four combination patterns can be specified with regard to land cover  
302 types of  $U_c$  and  $U_n$  pixels: (1) vegetation surrounded by buildings (GB), (2) buildings  
303 surrounded by vegetation (BG), (3) buildings surrounded by buildings (BB), and (4) vegetation  
304 surrounded by vegetation (GG). The Gaussian kernel density fit of  $\widehat{SUHI}_{Ten}$  for each

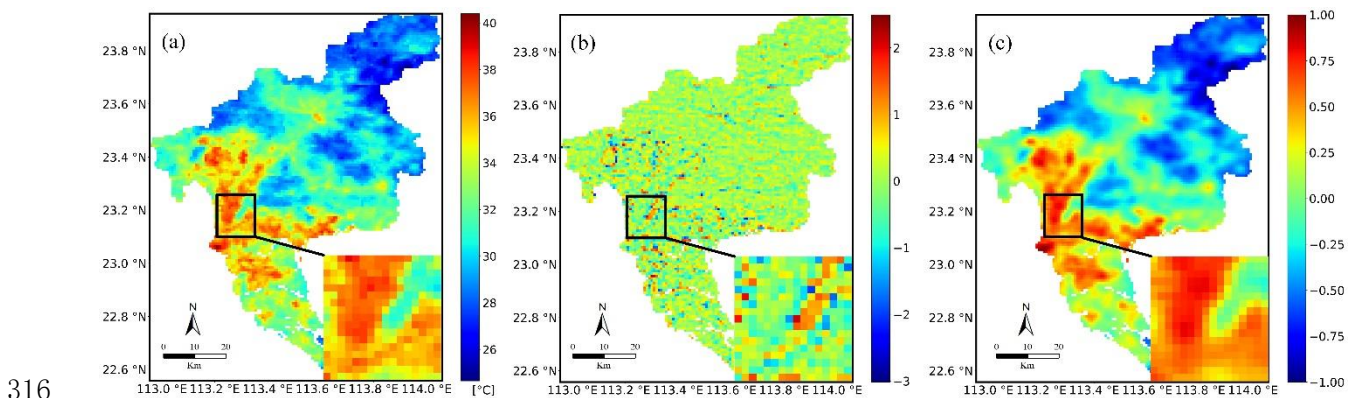
305 combination is then plotted to associate computed  $SUHI_{Ten}$  with land cover patterns, so that  
306 the effectiveness of  $SUHI_{Ten}$  can be verified.

## 307 Results

### 308 A. LST, local SUHII, and $SUHI_{Ten}$

309 The original LST, local SUHII variation (intermediate results), and final  $SUHI_{Ten}$  results are  
310 illustrated in Fig. 3. The maximum LST is 40.40°C, and the minimum LST is 24.64°C during  
311 the summer season of 2015. Clearly, higher LST values are concentrated in Guangzhou's urban  
312 extent that is mainly covered by buildings and impervious surface (Fig. 2), and LST decreases  
313 from urbanized region toward urban periphery and countryside areas (Fig. 3a) that are largely  
314 covered by croplands and various forests (Fig. 2).

315



317 Fig. 3. (a) Original LST, (b) Local SUHII variation, (c)  $SUHI_{Ten}$ , based on a mosaic of  
318 MODIS thermal images

319

320 When the magnitude of local SUHII variation portrayed by Fig. 3b is considered, significant  
321 SUHII variations can be detected across the whole city, shown as red pixels with positive

322 sharpening or blue pixels with negative sharpening, even though a planar SHUII pattern  
323 dominates, shown as green pixels with zero SUHII variation. The dominant planar SUHII is  
324 resulted from consistent thermal property of land cover between center pixels and their  
325 neighboring pixels, while the red and blue pixels reveal neighboring pixels' heating and cooling  
326 impacts, respectively. These local SUHII variations are sensitive to the spatial composition and  
327 configuration of a center pixel's land cover type and that of its eight neighbors. The significant  
328 variation of locally sharpened SUHII reflects the existence of interactive influence within this  
329 micro thermal environment (covering a center pixel and its eight neighboring pixels) across the  
330 study area resulted from land cover homogeneity (exacerbating UHI or UCI) or heterogeneity  
331 (mitigating UHI or UCI). As illustrated by a region containing dense buildings and an urban  
332 park (specified by the square in Fig. 3), pixels located at the interface exhibit significant SHUII  
333 variations, either negative (displayed with blue tone) or positive (displayed with red tone),  
334 resulted from land cover characteristics of their neighboring pixels and their direct influence on  
335 ground thermal thermodynamics between the center pixel and its neighbors. For example,  
336 abundant vegetation in neighboring pixels would significantly cool down the central pixel that  
337 is covered mainly by buildings through thermal conduction and convection (Deng and Wu 2013;  
338 Kim and Guldmann 2014; Weng et al. 2004).

339

340 Combining this pixel-level SUHI variation with its original LST to generate  $\widehat{SUHII}_{ten}$  would  
341 therefore successfully retain not only the overall thermal context across the city (as reflected  
342 by the original LST), but also capture local variability and interactive mechanisms of inter-  
343 pixel thermal patterns. Fig. 3c visualizes the estimated  $\widehat{SUHII}_{ten}$ . A simple visual examination

344 of Fig. 3c and Fig 3a (retrieved original LST) reveals a similar distribution pattern of UHI.  
345 Pixels with negative  $\widehat{SUHI}_{Ten}$  are mainly found in non-urbanized areas, covered by different  
346 types of vegetation. In comparison, pixels with positive  $\widehat{SUHI}_{Ten}$  are observed inside of urban  
347 core areas, which are covered by dense buildings and impervious surfaces. Notably, detailed  
348 thermal information reflecting thermal transitions at the boundary separating different land uses  
349 can also be found in Fig. 3c, instead of sudden breaks and sharp contrasts between different  
350 land surface and thermal properties as portrayed in Fig. 3a. Meanwhile,  $\widehat{SUHI}_{Ten}$  makes more  
351 pronounced some spots that are not only heat per se (with higher original LST), but also receive  
352 additional heat load emitted from directly adjacent pixels (when they are hotter than the central  
353 pixel, and thus a positive  $C$ ). Special attention should be paid to these pixels, as more serious  
354 health impacts might be triggered for local residents, so that site-specific mitigation strategies  
355 should be formulated. On the contrary, even though some spots are specified as heat islands as  
356 indicated by their high LST, their heat load might be moderated via the cooling effect induced  
357 by their neighboring pixels (which exhibit significantly lower LST, thus a negative  $C$ ), and thus  
358 these spots might not be sites necessitating immediate attention for UHI mitigation.

359

#### 360 *B. Verification of $\widehat{SUHI}_{Ten}$ using original LST and land use patterns*

361 In addition to simple visual examination and comparison, two measurements (using the original  
362 LST and land use patterns) are applied to further validate the effectiveness of computed  
363  $\widehat{SUHI}_{Ten}$ .

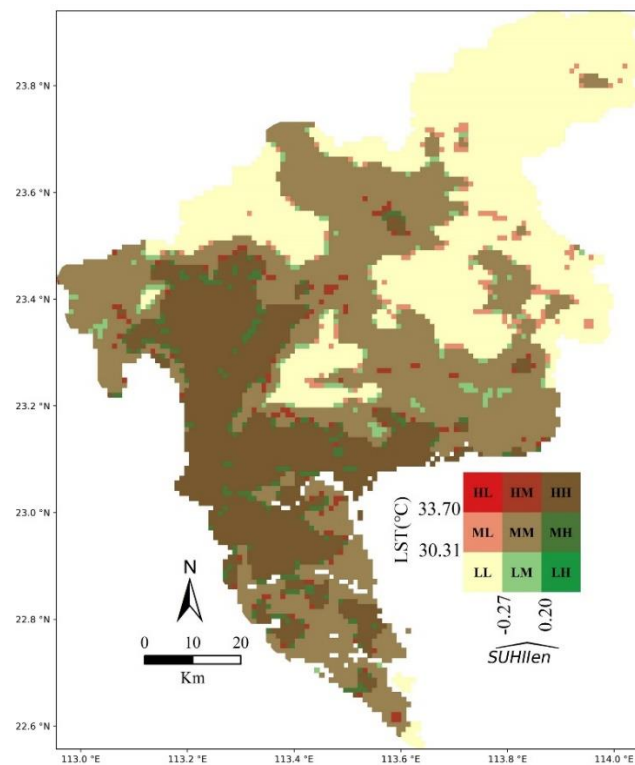
364

365 Firstly, a simple ordinary least squares regression is conducted to check the correlation between  
366 the original LST and the estimated  $\widehat{SUHI}_{ten}$  for each pixel, with a result of  $R^2$  at 0.969. On  
367 the one hand, this result suggests that  $\widehat{SUHI}_{ten}$  is a highly effective indicator applicable in  
368 explaining the LST and thus urban heat island phenomenon. On the other hand, this result also  
369 reveals the existence of discrepancy between the LST and  $\widehat{SUHI}_{ten}$ . To further detect the  
370 locational concordance and discordance between the original LST and  $\widehat{SUHI}_{ten}$  in the spatial  
371 context of the study area, a bivariate choropleth map is created (Fig. 4). This bivariate map  
372 allows for the visualization of two features (LST and  $\widehat{SUHI}_{ten}$ ) in a single map by displaying  
373 each feature with a distinct color gradient, whereby the tonally additive result of the overlapping  
374 gradients can describe each pixels' degree of concordance or discordance between the LST  
375 and  $\widehat{SUHI}_{ten}$  (Nöllenburg 2007). In this map, a 9-class sequential color scheme with the LST  
376 and  $\widehat{SUHI}_{ten}$  being categorized into three classes: low (L), medium (M), and high (H), such  
377 that when these two indicators for each pixel are compared, all combination patterns could be  
378 reflected using this 9-class sequential color scheme. The cut-off points within each feature are  
379 determined using the Jenks natural breaks classification method (Jenks and Caspall 1971),  
380 which can minimize each class's average deviation from the class mean and maximize each  
381 class's deviation from the means of other classes (Chen et al. 2013).

382

383 Overall, the bivariate map showing the spatial concordance between the LST and  $\widehat{SUHI}_{ten}$   
384 highlights three distinctive regions (Fig. 4): urban context with high LST and high  $\widehat{SUHI}_{ten}$   
385 (HH region), urban periphery with medium LST and medium  $\widehat{SUHI}_{ten}$  (MM region), and  
386 countryside area with low LST and low  $\widehat{SUHI}_{ten}$  (LL region). More importantly, this

387 bivariate map also reveals unequivocally the spatial discordance between the LST and  
 388  $\widehat{SUHI}_{ten}$ , revealing far more complicated micro-thermal situations resulted from pixel-level  
 389 thermodynamics existing at not only the transitional zones of the urban-periphery-countryside  
 390 continuum, but also within urban context, periphery zone, as well as rural area. The HL, HM,  
 391 and ML pixel locations manifest moderating/cooling effect introduced by neighboring pixels,  
 392 while the LH, LM and MH locations show the reinforcing/heating effect brought by  
 393 neighboring pixels. The spatially explicit detection of these LST- $\widehat{SUHI}_{ten}$  discordance  
 394 locations is of pivotal importance, as for these pixels, distorted interpretations of surface urban  
 395 heat island characteristics would be derived if judging solely based on individual pixels' LST  
 396 information without taking neighboring pixels' thermal influences into account.



397  
 398 Fig. 4. A 9-class bivariate map showing the concordance/discordance between LST and  
 399  $\widehat{SUHI}_{ten}$

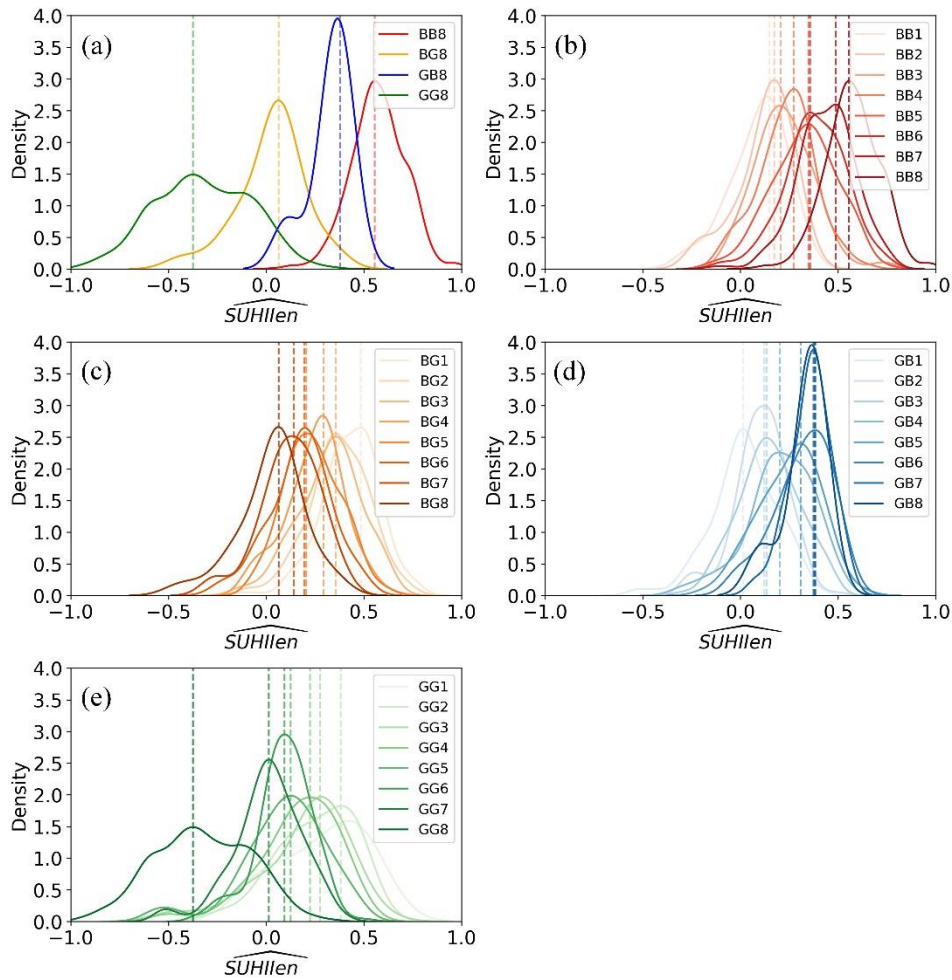
400

401 Secondly, the effectiveness of  $\widehat{SUHI}_{ten}$  is double-checked with respect to the land use  
402 patterns of the center pixel and neighboring pixels, which have been empirically used to  
403 interpret SUHII spatial characteristics (Bokaie et al. 2016; Chen et al. 2006; Zhou and Chen  
404 2018). We also plot the distribution of  $\widehat{SUHI}_{ten}$  occurrences (Gaussian density curve) for  
405 different land use patterns in the study area (see Fig. 5). Four typical land use patterns are  
406 considered in Fig. 5a, including BB8 (the center pixel with building/imperious surface,  
407 surrounded by 8 neighboring pixels with the same building/imperious surface), BG8 (the center  
408 pixel with building/imperious surface, surrounded by 8 neighboring pixels with vegetation  
409 coverage), GB8 (the center pixel with vegetation coverage, surrounded by 8 neighboring pixels  
410 with building/imperious surface) and GG8 (the center pixel with vegetation coverage,  
411 surrounded by 8 neighboring pixels with the same vegetation surface). The peak  $\widehat{SUHI}_{ten}$   
412 value (the most probable value) increases from GG8 (-0.375), to BG8 (0.064), GB8 (0.379),  
413 and BB8 (0.556). This trend corroborates that  $\widehat{SUHI}_{ten}$  can adequately take into account the  
414 thermal properties and interactions between the central and neighboring pixels, as lower  
415  $\widehat{SUHI}_{ten}$  values are associated with more vegetation coverage and the cooling effect of this  
416 land use type), and higher  $\widehat{SUHI}_{ten}$  values are associated with more building and imperious  
417 surface and the heating effect of this land use type.

418

419 A further step in this verification process is to assess Gaussian density curve with stepwise  
420 increments of the thermal influence from neighboring pixels. Fig. 5b and Fig. 5c illustrate the  
421 Gaussian densities for the center pixels with building/imperious surface. Clearly, Fig. 5b  
422 reveals that the peak  $\widehat{SUHI}_{ten}$  value increases when the number of building-covered

423 neighboring pixels increases from 1 to 8 within the Laplacian kernel, while Fig. 5c shows the  
424 peak  $\widehat{SUHTIen}$  value decreases, when the number of vegetation-covered neighboring pixels  
425 increases from 1 to 8. Similarly, Fig. 5d and Fig 5e illustrate the Gaussian densities for the  
426 center pixels with vegetation surface. The peak  $\widehat{SUHTIen}$  value increases with an increase of  
427 the number of building-covered neighboring pixels (Fig. 5d), decreases with an increase of the  
428 number of vegetation-covered neighboring pixels (Fig. 5e). These results imply the heating  
429 effect exerted by building/imperious surface and the cooling effect by vegetation in close  
430 proximity, thus lend additional support to the effectiveness of the computed  $\widehat{SUHTIen}$ , even  
431 though potential thermal anisotropy associated with land configuration such as building  
432 geometry/orientation, urban canyon structure, and vegetation structure/density (Voogt and Oke  
433 2003) that might determine the magnitude of neighboring pixels' thermal influence is not  
434 considered in this verification process.



435

436 Fig. 5. (a) Gaussian density fit curve of  $SUHII_{ten}$  for four typical land use patterns (BB4, BG4,

437 GB4, and GG4); (b)-(e) Gaussian density fit curve of  $SUHII_{ten}$  for the stepwise increments of

438 the thermal influence from neighboring pixels for four typical land use patterns (BB, BG, GB,

439 and GG)

440

#### 441 **Conclusion**

442 Even though LST retrieved from thermal satellite images provides a valuable means to

443 understand urban heat island phenomenon due to consistent periodicity, high-spatial resolution,

444 and global coverage (Lai et al. 2018; Rao 1972; Voogt and Oke 2003; Zhou and Chen 2018),

445 how to adequately explain the thermal characteristics and spatial patterns using LST data across

446 the urban-periphery-rural continuum has been challenging (Deng and Wu 2013; Keramitsoglou  
447 et al. 2011; Weng et al. 2004). This paper presents an innovative attempt to quantify a new  
448 SHUI indicator,  $\widehat{SUHI}_{en}$  (enhanced SUHI intensity), and to test the effectiveness of  
449  $\widehat{SUHI}_{en}$  using a demonstrative case study. This  $\widehat{SUHI}_{en}$  integrates a pixel's LST  
450 magnitude that reflects a city's overall thermal context with its thermal characteristics that takes  
451 the influence of neighboring pixels into account via a pixel-based sharpening enhancement  
452 approach. Different from the original LST or urban-rural LST comparison that have been  
453 empirically used to characterize UHI phenomenon (Deilami et al. 2018; Li et al. 2018; Li et al.  
454 2020b; Streutker 2002), this  $\widehat{SUHI}_{en}$  can be computed for the whole urban-periphery-rural  
455 continuum, and eliminate the biases caused by the selection of non-representative pixels of  
456 urban and rural areas. It embraces Tobler's first law of geography (everything is related to  
457 everything else, but near things are more related than distant things) (Tobler 1970) by  
458 highlighting how neighboring pixels' homogenous/heterogeneous land cover and associated  
459 thermal properties could affect center pixels' thermal characteristics via either reinforcement  
460 or mitigation of heat load. While the conventional SUHI based on urban-rural LST comparison  
461 possesses clear physical meaning that explains LST gradient difference between urban and rural  
462 areas,  $\widehat{SUHI}_{en}$  is computed via a physically based method thus also with explicit physical  
463 meaning. It is able to connote latent thermal interactions at pixel level and specify relatively  
464 heat areas ( $0 < \widehat{SUHI}_{en} \leq 1$ ) and relatively cold areas ( $-1 \leq \widehat{SUHI}_{en} < 0$ ) as compared  
465 with the average condition across the whole city. Thus  $\widehat{SUHI}_{en}$  provides a more in-depth  
466 understanding of pixel-level UHI phenomenon across a study area that has complex and

467 heterogeneous land cover and land use, and promises rigorous assessment of potential UHI  
468 effects and cognate risks.

469 This  $\widehat{SUHI}_{ten}$  can be further expanded into two directions. This study uses only day time LST  
470 for summer season to construct and test  $\widehat{SUHI}_{ten}$ . Therefore it is necessary to check the  
471 feasibility and effectiveness of  $\widehat{SUHI}_{ten}$  for explaining UHI during night time and different  
472 seasons. Additionally, different land use types are grouped into two broad categories in this  
473 study, i.e. building/imperious surface, and vegetation. Thus it is not clear how spatial  
474 configuration of urban surface structure and land use patterns at finer scales might affect pixel-  
475 level thermodynamic properties and also the computation of  $\widehat{SUHI}_{ten}$ . In this regard, a  
476  $\widehat{SUHI}_{ten}$  adjusted for multiple satellite sensors and more detailed land use patterns might be  
477 a promising solution for quantifying SUHI magnitude.

478

#### 479 **Acknowledgment**

480 The authors wish to thank two anonymous reviewers as well as the editor for their helpful  
481 comments and suggestions.

482

483

#### 484 **References**

- 485 Anniballe R, Bonafoni S, Pichierri M (2014) Spatial and temporal trends of the surface and air  
486 heat island over Milan using MODIS data. *Remote Sensing of Environment* 150:163-171  
487 Basu M (2002) Gaussian-based edge-detection methods-a survey. *IEEE Transactions on*  
488 *Systems, Man, and Cybernetics, Part C (Applications and Reviews)* 32(3):252-260  
489 Bian L, Butler R (1999) Comparing effects of aggregation methods on statistical and spatial  
490 properties of simulated spatial data. *Photogrammetric engineering and remote sensing*  
491 65:73-84

492 Bokaie M, Zarkesh MK, Arasteh PD, Hosseini A (2016) Assessment of urban heat island based  
493 on the relationship between land surface temperature and land use/land cover in Tehran.  
494 *Sustainable Cities and Society* 23:94-104

495 Bonafoni S, Baldinelli G, Verducci P (2017) Sustainable strategies for smart cities: Analysis of  
496 the town development effect on surface urban heat island through remote sensing  
497 methodologies. *Sustainable Cities and Society* 29:211-218

498 Buyantuyev A, Wu J (2010) Urban heat islands and landscape heterogeneity: linking  
499 spatiotemporal variations in surface temperatures to land-cover and socioeconomic  
500 patterns. *Landscape ecology* 25(1):17-33

501 Canny J (1986) A computational approach to edge detection. *IEEE Transactions on pattern  
502 analysis and machine intelligence*(6):679-698

503 Chakraborty T, Lee X (2019) A simplified urban-extent algorithm to characterize surface urban  
504 heat islands on a global scale and examine vegetation control on their spatiotemporal  
505 variability. *International Journal of Applied Earth Observation and Geoinformation*  
506 74:269-280

507 Chao L, Huang B, Yuanjian Y et al (2020) A new evaluation of the role of urbanization to  
508 warming at various spatial scales: Evidence from the Guangdong-Hong Kong-Macau  
509 region, China. *Geophysical Research Letters* 47(20):e2020GL089152

510 Chen J, Yang S, Li H, Zhang B, Lv J (2013) Research on geographical environment unit  
511 division based on the method of natural breaks (Jenks). *Int. Arch. Photogramm. Remote  
512 Sens. Spat. Inf. Sci* 3:47-50

513 Chen X-L, Zhao H-M, Li P-X, Yin Z-Y (2006) Remote sensing image-based analysis of the  
514 relationship between urban heat island and land use/cover changes. *Remote sensing of  
515 environment* 104(2):133-146

516 Deilami K, Kamruzzaman M, Liu Y (2018) Urban heat island effect: A systematic review of  
517 spatio-temporal factors, data, methods, and mitigation measures. *International journal of  
518 applied earth observation and geoinformation* 67:30-42

519 Deng C, Wu C (2013) Examining the impacts of urban biophysical compositions on surface  
520 urban heat island: A spectral unmixing and thermal mixing approach. *Remote Sensing of  
521 Environment* 131:262-274

522 Dhal KG, Ray S, Das A, Das S (2019) A survey on nature-inspired optimization algorithms and  
523 their application in image enhancement domain. *Archives of Computational Methods in  
524 Engineering* 26(5):1607-1638

525 Duan S-B, Li Z-L (2016) Spatial downscaling of MODIS land surface temperatures using  
526 geographically weighted regression: Case study in northern China. *IEEE Transactions on  
527 Geoscience and Remote Sensing* 54(11):6458-6469

528 Feng X, Foody G, Aplin P, Gosling SN (2015) Enhancing the spatial resolution of satellite-  
529 derived land surface temperature mapping for urban areas. *Sustainable Cities and Society*  
530 19:341-348

531 Fu S, Ruan Q, Wang W Remote sensing image data enhancement based on robust inverse  
532 diffusion equation for agriculture applications. In, 2008. *IEEE*, p. 1231-1234

533 Gorelick N, Hancher M, Dixon M, Ilyushchenko S, Thau D, Moore R (2017) Google Earth  
534 Engine: Planetary-scale geospatial analysis for everyone. *Remote sensing of  
535 Environment* 202:18-27

536 Guo A, Yang J, Sun W et al (2020) Impact of urban morphology and landscape characteristics  
537 on spatiotemporal heterogeneity of land surface temperature. *Sustainable Cities and*  
538 *Society* 63:102443

539 Guo G, Wu Z, Xiao R, Chen Y, Liu X, Zhang X (2015) Impacts of urban biophysical  
540 composition on land surface temperature in urban heat island clusters. *Landscape and*  
541 *Urban Planning* 135:1-10

542 Han L, Liu Z, Ning Y, Zhao Z (2018) Extraction and analysis of geological lineaments  
543 combining a DEM and remote sensing images from the northern Baoji loess area.  
544 *Advances in Space Research* 62(9):2480-2493

545 Haralick RM (1987) Digital step edges from zero crossing of second directional derivatives.  
546 *Readings in Computer Vision*. Elsevier, pp. 216-226

547 Jeevakala S (2018) Sharpening enhancement technique for MR images to enhance the  
548 segmentation. *Biomedical Signal Processing and Control* 41:21-30

549 Jenerette GD, Harlan SL, Buyantuev A et al (2016) Micro-scale urban surface temperatures are  
550 related to land-cover features and residential heat related health impacts in Phoenix, AZ  
551 USA. *Landscape Ecology* 31(4):745-760

552 Jenks GF, Caspall FC (1971) Error on choroplethic maps: definition, measurement, reduction.  
553 *Annals of the Association of American Geographers* 61(2):217-244

554 Keramitsoglou I, Kiranoudis CT, Ceriola G, Weng Q, Rajasekar U (2011) Identification and  
555 analysis of urban surface temperature patterns in Greater Athens, Greece, using MODIS  
556 imagery. *Remote Sensing of Environment* 115(12):3080-3090

557 Kim J-P, Guldmann J-M (2014) Land-use planning and the urban heat island. *Environment and*  
558 *Planning B: Planning and Design* 41(6):1077-1099

559 Kwarteng P, Chavez A (1989) Extracting spectral contrast in Landsat Thematic Mapper image  
560 data using selective principal component analysis. *Photogramm. Eng. Remote Sens*  
561 *55(1):339-348*

562 Lai J, Zhan W, Huang F et al (2018) Does quality control matter? Surface urban heat island  
563 intensity variations estimated by satellite-derived land surface temperature products.  
564 *ISPRS Journal of photogrammetry and Remote Sensing* 139:212-227

565 Lai J, Zhan W, Voogt J et al (2021) Meteorological controls on daily variations of nighttime  
566 surface urban heat islands. *Remote Sensing of Environment* 253:112198

567 Li G, Wang Q Research on Reefs Extraction Method Based on Multi-spectral Remote Sensing.  
568 In, 2013. IEEE, p. 14-17

569 Li H, Zhou Y, Li X et al (2018) A new method to quantify surface urban heat island intensity.  
570 *Science of the total environment* 624:262-272

571 Li J, Wang F, Fu Y, Guo B, Zhao Y, Yu H (2020a) A novel SUHI referenced estimation method  
572 for multicenters urban agglomeration using DMSP/OLS nighttime light data. *IEEE*  
573 *Journal of Selected Topics in Applied Earth Observations and Remote Sensing* 13:1416-  
574 1425

575 Li K, Chen Y, Wang M, Gong A (2019) Spatial-temporal variations of surface urban heat island  
576 intensity induced by different definitions of rural extents in China. *Science of the Total*  
577 *Environment* 669:229-247

578 Li L, Zha Y, Zhang J (2020b) Spatially non-stationary effect of underlying driving factors on  
579 surface urban heat islands in global major cities. *International Journal of Applied Earth*  
580 *Observation and Geoinformation* 90:102131

581 Li N, Li X (2020) The impact of building thermal anisotropy on surface urban heat island  
582 intensity estimation: An observational case study in Beijing. *IEEE Geoscience and*  
583 *Remote Sensing Letters* 17(12):2030-2034

584 Li Q, Dong W (2009) Detection and adjustment of undocumented discontinuities in Chinese  
585 temperature series using a composite approach. *Advances in Atmospheric Sciences*  
586 26(1):143-153

587 Li W, Cao Q, Lang K, Wu J (2017) Linking potential heat source and sink to urban heat island:  
588 Heterogeneous effects of landscape pattern on land surface temperature. *Science of the*  
589 *Total Environment* 586:457-465

590 Li Y-y, Zhang H, Kainz W (2012) Monitoring patterns of urban heat islands of the fast-growing  
591 Shanghai metropolis, China: Using time-series of Landsat TM/ETM+ data. *International*  
592 *Journal of Applied Earth Observation and Geoinformation* 19:127-138

593 Lu Y, Wu P, Ma X, Yang H, Wu Y (2020) Monitoring seasonal and diurnal surface urban heat  
594 islands variations using Landsat-scale data in Hefei, China, 2000–2017. *IEEE Journal of*  
595 *Selected Topics in Applied Earth Observations and Remote Sensing* 13:6410-6423

596 Ma J, Yu W, Chen C, Liang P, Guo X, Jiang J (2020) Pan-GAN: An unsupervised pan-  
597 sharpening method for remote sensing image fusion. *Information Fusion* 62:110-120

598 Mahmoud SH, Alazba AA (2016) Integrated remote sensing and GIS-based approach for  
599 deciphering groundwater potential zones in the central region of Saudi Arabia.  
600 *Environmental Earth Sciences* 75(4):344

601 Marr D, Hildreth E (1980) Theory of edge detection. *Proceedings of the Royal Society of*  
602 *London. Series B. Biological Sciences* 207(1167):187-217

603 Meng Q, Zhang L, Sun Z, Meng F, Wang L, Sun Y (2018) Characterizing spatial and temporal  
604 trends of surface urban heat island effect in an urban main built-up area: A 12-year case  
605 study in Beijing, China. *Remote Sensing of Environment* 204:826-837

606 Nöllenburg M (2007) Geographic visualization. *Human-centered visualization environments*.  
607 Springer, pp. 257-294

608 Oke TR (1982) The energetic basis of the urban heat island. *Quarterly Journal of the Royal*  
609 *Meteorological Society* 108(455):1-24

610 Peng J, Hu Y, Dong J, Liu Q, Liu Y (2020) Quantifying spatial morphology and connectivity  
611 of urban heat islands in a megacity: a radius approach. *Science of The Total Environment*  
612 714:136792

613 Peng S, Piao S, Ciais P et al (2012) Surface urban heat island across 419 global big cities.  
614 *Environmental science & technology* 46(2):696-703

615 Pereira Filho AJ, Karam HA (2016) Estimation of long term low resolution surface urban heat  
616 island intensities for tropical cities using MODIS remote sensing data. *Urban Climate*  
617 17:32-66

618 Prewitt JMS (1970) Object enhancement and extraction. *Picture processing and*  
619 *Psychopictorics* 10(1):15-19

620 Rajasekar U, Weng Q (2009) Urban heat island monitoring and analysis using a non-parametric  
621 model: A case study of Indianapolis. *ISPRS Journal of Photogrammetry and Remote*  
622 *Sensing* 64(1):86-96

623 Rao PK (1972) Remote sensing of urban "heat islands" from an environmental satellite. *Bulletin*  
624 *of the American meteorological society* 53(7):647-648

625 Rasul A, Balzter H, Smith C et al (2017) A review on remote sensing of urban heat and cool  
626 islands. *Land* 6(2):38

627 Ratcliffe CP (1997) Damage detection using a modified Laplacian operator on mode shape data.  
628 *Journal of Sound and Vibration* 204(3):505-517

629 Roberts LG (1963) Machine perception of three-dimensional solids.

630 Schwarz N, Lautenbach S, Seppelt R (2011) Exploring indicators for quantifying surface urban  
631 heat islands of European cities with MODIS land surface temperatures. *Remote Sensing*  
632 *of Environment* 115(12):3175-3186

633 Sekertekin A, Zadbagher E (2021) Simulation of future land surface temperature distribution  
634 and evaluating surface urban heat island based on impervious surface area. *Ecological*  
635 *Indicators* 122:107230

636 Shen Y, Shen H, Cheng Q, Zhang L (2020) Generating Comparable and Fine-Scale Time Series  
637 of Summer Land Surface Temperature for Thermal Environment Monitoring. *IEEE*  
638 *Journal of Selected Topics in Applied Earth Observations and Remote Sensing* 14:2136-  
639 2147

640 Smoliak BV, Snyder PK, Twine TE, Mykleby PM, Hertel WF (2015) Dense network  
641 observations of the Twin Cities canopy-layer urban heat island. *Journal of Applied*  
642 *Meteorology and Climatology* 54(9):1899-1917

643 Sobel I, Feldman G (1968) A 3x3 isotropic gradient operator for image processing. a talk at the  
644 Stanford Artificial Project in:271-272

645 Stewart ID, Oke TR (2012) Local Climate Zones for Urban Temperature Studies. *Bulletin of*  
646 *the American Meteorological Society* 93(12):1879-1900

647 Streutker DR (2002) A remote sensing study of the urban heat island of Houston, Texas.  
648 *International Journal of Remote Sensing* 23(13):2595-2608

649 Streutker DR (2003) Satellite-measured growth of the urban heat island of Houston, Texas.  
650 *Remote Sensing of Environment* 85(3):282-289

651 Tobler WR (1970) A computer movie simulating urban growth in the Detroit region. *Economic*  
652 *geography* 46(sup1):234-240

653 Torre V, Poggio TA (1986) On edge detection. *IEEE Transactions on Pattern Analysis and*  
654 *Machine Intelligence*(2):147-163

655 Tran H, Uchihama D, Ochi S, Yasuoka Y (2006) Assessment with satellite data of the urban  
656 heat island effects in Asian mega cities. *International journal of applied Earth observation*  
657 *and Geoinformation* 8(1):34-48

658 Voogt JA, Oke TR (2003) Thermal remote sensing of urban climates. *Remote sensing of*  
659 *environment* 86(3):370-384

660 Waleed M, Um T-W, Khan A, Ahmad Z (2020) An Automated Method for Detection and  
661 Enumeration of Olive Trees Through Remote Sensing. *IEEE Access* 8:108592-108601

662 Wan Z, Zhang Y, Zhang Q, Li ZL (2004) Quality assessment and validation of the MODIS  
663 global land surface temperature. *International journal of remote sensing* 25(1):261-274

- 664 Wang R, Cai M, Ren C, Bechtel B, Xu Y, Ng E (2019) Detecting multi-temporal land cover  
665 change and land surface temperature in Pearl River Delta by adopting local climate zone.  
666 *Urban Climate* 28:100455
- 667 Wang W, Liang S, Meyers T (2008) Validating MODIS land surface temperature products  
668 using long-term nighttime ground measurements. *Remote Sensing of Environment*  
669 112(3):623-635
- 670 Weng Q (2009) Thermal infrared remote sensing for urban climate and environmental studies:  
671 Methods, applications, and trends. *ISPRS Journal of photogrammetry and remote sensing*  
672 64(4):335-344
- 673 Weng Q, Lu D, Schubring J (2004) Estimation of land surface temperature–vegetation  
674 abundance relationship for urban heat island studies. *Remote sensing of Environment*  
675 89(4):467-483
- 676 Weng Q, Rajasekar U, Hu X (2011) Modeling urban heat islands and their relationship with  
677 impervious surface and vegetation abundance by using ASTER images. *IEEE*  
678 *Transactions on Geoscience and Remote Sensing* 49(10):4080-4089
- 679 Xiao R, Weng Q, Ouyang Z, Li W, Schienke EW, Zhang Z (2008) Land surface temperature  
680 variation and major factors in Beijing, China. *Photogrammetric Engineering & Remote*  
681 *Sensing* 74(4):451-461
- 682 Yang Q, Huang X, Tang Q (2019) The footprint of urban heat island effect in 302 Chinese  
683 cities: Temporal trends and associated factors. *Science of the Total Environment*  
684 655:652-662
- 685 Yang Z, Witharana C, Hurd J, Wang K, Hao R, Tong S (2020) Using Landsat 8 data to compare  
686 percent impervious surface area and normalized difference vegetation index as indicators  
687 of urban heat island effects in Connecticut, USA. *Environmental Earth Sciences*  
688 79(18):1-13
- 689 Yu R, Fu X, Jiang H et al Remote Sensing Image Segmentation by Combining Feature  
690 Enhanced with Fully Convolutional Network. In, 2018. Springer, p. 406-415
- 691 Yu Z, Fryd O, Sun R et al (2021) Where and how to cool? An idealized urban thermal security  
692 pattern model. *Landscape Ecology* 36(7):2165-2174
- 693 Zhan W, Chen Y, Zhou J et al (2013) Disaggregation of remotely sensed land surface  
694 temperature: Literature survey, taxonomy, issues, and caveats. *Remote Sensing of*  
695 *Environment* 131:119-139
- 696 Zhang Y, Cheng J (2019) Spatio-temporal analysis of urban heat island using multisource  
697 remote sensing data: A case study in Hangzhou, China. *IEEE Journal of Selected Topics*  
698 *in Applied Earth Observations and Remote Sensing* 12(9):3317-3326
- 699 Zhao C, Jensen J, Weng Q, Weaver R (2018) A geographically weighted regression analysis of  
700 the underlying factors related to the surface urban heat island phenomenon. *Remote*  
701 *Sensing* 10(9):1428
- 702 Zhao L, Lee X, Smith RB, Oleson K (2014) Strong contributions of local background climate  
703 to urban heat islands. *Nature* 511(7508):216-219
- 704 Zhou D, Xiao J, Bonafoni S et al (2019) Satellite remote sensing of surface urban heat islands:  
705 Progress, challenges, and perspectives. *Remote Sensing* 11(1):48

706 Zhou X, Chen H (2018) Impact of urbanization-related land use land cover changes and urban  
707 morphology changes on the urban heat island phenomenon. *Science of the Total*  
708 *Environment* 635:1467-1476

709 **Declarations**

710 **Funding**

711 *This work was supported by HUK Foundation Postgraduate Fellowship.*

712

713 **Competing Interests**

714 *The authors have no relevant financial or non-financial interests to disclose.*

715

716 **Author Contributions**

717 *All authors contributed to the study conception and design. Data collection and analysis were*  
718 *performed by Yanhua Chen. The first draft of the manuscript was written by Wendy Y. Chen*  
719 *and Yanhua Chen. All authors commented on previous versions of the manuscript. All authors*  
720 *read and approved the final manuscript.*

721

722 **Ethical Statement**

723 *Hereby, all authors consciously assure that for our manuscript the following is fulfilled:*

724 *1) This material is the authors' own original work, which has not been previously published*  
725 *elsewhere.*

726 *2) The paper is not currently being considered for publication elsewhere.*

727 *3) The paper reflects the authors' own research and analysis in a truthful and complete*  
728 *manner.*

729 *4) The paper properly credits the meaningful contributions of co-authors and co-researchers.*

730 *5) The results are appropriately placed in the context of prior and existing research.*

731 *6) All sources used are properly disclosed.*

732 *7) All authors have been personally and actively involved in substantial work leading to the*  
733 *paper, and will take public responsibility for its content.*